IMPORTANCE OF MESOSCALE CURRENTS IN AMOC PATHWAYS AND TIMESCALES

Igor Kamenkovich[1]**,**

RSMAS, University of Miami, Miami, FL

and

Zulema Garraffo,

IMSG at NOAA/EMC, College Park, MD

[1] Corresponding author: Igor Kamenkovich. Email address: *ikamenkovich@miami.edu*

ABSTRACT

The Atlantic Meridional Overturning Circulation (AMOC) plays a key role in climate due to uptake and redistribution of heat and carbon anomalies. This redistribution takes place along several main pathways that link the high-latitude North Atlantic with mid-latitudes and the Southern Ocean and involves currents on a wide range of spatial scales. This numerical study examines the importance of mesoscale currents ("eddies") in these AMOC pathways and associated timescales, using a highly efficient offline tracer model. The study uses two Boundary Impulse Response (BIR) tracers, which can quantify the importance of the Atlantic tracer exchanges with the high-latitude atmosphere in the north and with the Southern Ocean in the south. The results demonstrate that mesoscale advection leads to an increase in the overall BIR inventory during the first 100 years and results in a more efficient and spatially uniform ventilation of the deep Atlantic. Mesoscale currents also facilitate meridional spreading of the BIR tracer and thus assist the large-scale advection. The results point toward the importance of spatial inhomogeneity and anisotropy of the eddy-induced mixing in several mixing "hot spots", as revealed by an eddy diffusivity tensor. Conclusions can be expected to assist evaluations of eddy-permitting simulations, that stop short of full resolution of mesoscale, as well as development of eddy parameterization schemes.

1 INTRODUCTION

Because of their enormous storage capacity, the oceans redistribute vast amounts of anomalous heat and carbon in the climate system and regulate long-term climate change. Model simulations further suggest that, on timescales of decades to centuries, the large-scale warming patterns are in large part controlled by the oceanic circulation, rather than the atmospheric processes (e.g., Marshall et al. 2015). The Atlantic Meridional Overturning Circulation (AMOC), defined here as an overall meridional flow in the Atlantic Ocean, plays a particularly important role in the Earth's climate and its variability (e.g., Broecker 1997; Stouffer et al. 2006). AMOC determines a large part of the oceanic uptake of heat and carbon and controls the depth to which these heat anomalies penetrate (e.g. Kuhlbrodt and Gregory 2012; Kostov et al. 2014). Studies further demonstrate that AMOC is different from a large-scale stationary "conveyor belt", but is rather a complex three-dimensional pattern (e.g. Lumpkin and Speer 2007), characterized by variability on a wide range of spatial and time scales (*e.g.* Smeed et al. 2014; Yeager and Danabasoglu 2014). In this paper, we will use high-resolution model simulations of dynamically passive tracers to better characterize the role of mesoscale currents (O[10-100 km] or "eddies" hereafter) in advective AMOC pathways and associated timescales.

Distribution of heat and anthropogenic carbon anomalies by AMOC is governed by complex interactions between the along- and cross-isopycnal advection and small-scale mixing. Diapycnal mixing can influence the mid-latitude stratification and high-latitude deep-water formation (e.g. Munk 1966; Gnanadesikan 1999), which is manifested in strong sensitivity of AMOC to vertical mixing in numerical simulations (e.g. Bryan 1987). In an alternative, semi-adiabatic regime (Marshall and Radko 2003), the water is moving strictly along isopycnals, forced by mass exchanges with the surface mixed layer. Several model-based studies suggest significance of a semi-adiabatic AMOC branch (Gnanadesikan 1999; Samelson 2004; Sevellec and Fedorov 2011; Toggweiler and Samuels 1998; Wolfe and Cessi 2010). Radko et al. (2008) describe this branch as a "push-pull mode" of AMOC and demonstrate that it explains most of the total AMOC transport and its variability (see also Grist et al. 2009; Han et al. 2013). The deep portion of the Atlantic push-pull mode is driven by the mass exchanges with the Southern Ocean and the deep mixed layer in the Northern high latitudes (Kamenkovich and Radko 2011; Radko et al. 2008).

The share of the semi-adiabatic component can be expected to be even larger in nature, since numerical simulations used in AMOC studies tend to have high values of diapycnal diffusivity, which are not supported by direct observational estimates (Ledwell et al. 1993; Toole et al. 1994).

The advective pathways outside of the mixed layer and convective sites are determined by interactions between large-scale currents and mesoscale eddies. Lateral transfer of buoyancy by mesoscale eddies have indeed been shown to play an active role in maintaining midlatitude stratification (Cessi and Fantini 2004; Henning and Vallis 2004; Radko and Marshall 2004) and propagation of the transient tracers (Booth and Kamenkovich 2008; Kamenkovich et al. 2017). In non-eddy-resolving simulations, the distributions of tracers and density is highly sensitive to horizontal resolution and parameterization of eddy-induced transports (e.g. Doney et al. 2004; Dutay et al. 2002; Gnanadesikan et al. 2013; Gnanadesikan et al. 2004; Sen Gupta and England 2004). Specifically, numerical simulations show strong sensitivity of the oceanic uptake of heat (*e.g.* Huang et al. 2003) and anthropogenic carbon (Gnanadesikan et al. 2015) to the horizontal and isopycnal eddy mixing.

The evolution of tracer anomalies entering the Atlantic from the surface and the Southern Ocean can be described as a response to the corresponding surface and lateral boundary forcing. A convenient way of calculating such a response involves the Boundary Impulse Response (BIR) function (Haine and Hall 2002; Holzer and Hall 2000; Khatiwala et al. 2001). For example, if the BIR is calculated from a response to an instant impulse at a given time and infinitely small surface area, it is equivalent to a Green's function. Such a Green function can in theory be calculated for all possible surface impulses. The concentration of an arbitrary tracer that enters the ocean through the surface and has no internal sources and sinks can then be derived from the tracer distribution at the surface and a complete set of BIRs. In practice, however, both the duration of the impulse and the source region area are made finite (*e.g.* Haine and Hall 2002; Khatiwala et al. 2001; Peacock and Maltrud 2006). For example, Khatiwala et al. (2009) used this approach to reconstruct the spatial distribution of anthropogenic carbon inventory. Mixing by eddies and small-scale processes can substantially modify the propagation of a pulse. Waugh and Hall (2005) used an idealized model of a deep western boundary current to demonstrate that

the arrival of the BIR peak value (the "pulse") can be significantly delayed by the mixing between the boundary current and the oceanic interior. Time scales in their model also strongly depend on the tracer time history at the origin, particularly in the intermediate mixing regime with comparable advective and mixing time scales (Peclet number of O(1)). Simulations of an ensemble of BIRs in a realistic global eddy-resolving model by Maltrud et al. (2010) exhibit vigorous mesoscale variability in BIR distributions but also demonstrate a remarkable agreement between ensemble members, especially at long timescales. In this paper, we will extend the previous studies and seek to isolate the importance of mesoscale eddies in AMOC advection by comparing two specific BIR simulations with and without mesoscale currents. A complete set of BIRs will not, however, be calculated.

The eddy-induced mixing of oceanic tracers is spatially inhomogeneous and anisotropic (e.g. Abernathey and Marshall 2013; Bachman et al. 2020; Kamenkovich et al. 2021; Rypina et al. 2012), which has been shown to be important for tracer distributions. For example, Booth and Kamenkovich (2008) used high-resolution simulations of the chloroflourocarbon-11 (CFC-11) with and without eddies to demonstrate the importance of eddy mixing in several key locations and show that eddies fill the interior of the Atlantic subpolar gyre with CFC-11, dispersing the tracer away from the mean pathways of the North Atlantic and Labrador currents; the eddies also act to limit vertical penetration of the tracer and decrease the convective removal of CFC-11 from the surface. Kamenkovich et al. (2017) used high-resolution simulations of a BIR tracer to study the interactions between the mean and eddy-induced advection in the Southern Ocean and show that the eddies spread the ventilation signal away from the mean pathways, which inhibits the removal of tracers from the Atlantic into the Indian Ocean and enhances the ventilation of the Atlantic southern subtropical gyre. Finally, the anisotropy of the mesoscale currents and the resulting eddy-induced transport are also important for tracer distribution within subtropical and subpolar gyres (Kamenkovich et al. 2015).

In this paper, we will use an offline tracer model of the Atlantic basin, whose high spatial resolution and numerical efficiency enables a direct inquiry into the importance of eddies in tracer distributions. We use BIR tracers, propagating from the North Atlantic surface and from the lateral southern boundary, to study the pathways and timescales associated with AMOC. We

do not calculate Transient Time Distribution (TTD) or ideal age of AMOC waters in this study, because it would require multiple simulations in a global domain. Instead, we focus on the importance of eddies in one realization of BIR evolution, assuming the results are representative (see Maltrud et al. 2010). The model is described in Section 2. The intensity of the eddy-induced stirring is quantified by a time-mean, but space-dependent diffusivity tensor in Section 3. Section 4 will compare the results in simulations with the full flow (hereafter FULL_ADV) and mean (large scale, hereafter, MEAN_ADV) flow only, which serves to isolate the direct importance of the eddy-induced tracer transports. Conclusions are drawn in Section 5.

2 ATLANTIC OFFLINE TRACER MODEL (AOTM)

The Atlantic Offline Tracer Model (AOTM) uses pre-calculated velocities, layer thicknesses and vertical diffusivities to solve the tracer equation. The formulation is similar to the one used in the Southern Ocean model by Kamenkovich et al. (2017) and will be only briefly described here. The physical variables are calculated in a separate "online" simulation with the HYbrid Coordinate Ocean Model (HYCOM; Bleck 2002; Chassignet et al. 2003; Halliwell 2004). HYCOM was originally based on the Miami Isopycnic Ocean Model (MICOM; Bleck et al. 1992) and uses isopycnal coordinates in the open ocean and below the mixed layer. The online simulation used by the AOTM has a global domain with 1/12^o spatial resolution; the horizontal grid is rectilinear south of 47^{o}N (being equatorial Mercator except in the high southern latitudes) followed by an Arctic bipolar patch. The vertical grid has 41 hybrid layers: isopycnal in the deep ocean, z-levels in the ocean interior near the surface, and sigma coordinates near the coasts. The horizontal resolution (~ 3.2–8km at 70^{o}S-30^{o}S) is among the highest available today, but still falls short of accurate resolution of the small-scale eddies of the size of the first internal Rossby deformation radius (~10-20 km at these latitudes; Chelton et al. 1998). Our focus is, therefore, on eddies with scales of larger than approximately 20-50 km. The potential density is referenced to the 20-MPa surface (Chassignet et al. 2003; Sun et al. 1999). The model employs the KPP vertical mixing scheme (Large et al. 1994), whose diapycnal/vertical coefficients are saved and used in AOTM.

The spinup for the base calculation was completed at the Naval Research Laboratory (NRL) starting from the observed stratification. The model was forced with monthly ECMWF (ERA40)

157 forcing fields plus 3 or 6-hourly anomalies obtained from NOGAPS. The ocean model is coupled
158 with the Los Alamos Sea Ice model (CICE). At this resolution, the model has been used
159 extensively at the NRL. Typically. a climatological spin up is used to initialize inter-annual
160 simulations; see http://www.hycom.org for more detail. The present climatological simulation
161 was spun up at NRL for 15 years and used for their Global Ocean Forecast System. This
162 simulation was run for additional 5 years and 16 days in order to save all the required fields,
163 including instantaneous horizontal mass fluxes and vertical diffusivities.

164 Off-line tracer simulations were originally formulated by R. Bleck (personal
165 communication); early off-line tracer simulations are presented in Sun and Bleck (2001). The
166 off-line tracer model solves the prognostic equation for the tracer concentration c within a layer
167 of thickness Δz(x,y,t) (Kamenkovich et al. 2017):

168 $$\frac{\partial(c\Delta z)}{\partial t} = -\nabla\cdot(\boldsymbol{U}c) - \partial(\omega c) + \nabla\cdot A_h\Delta z\nabla c + \mathfrak{D}(c) \qquad (1)$$

169 where $\mathfrak{D}(c)$ is the diapycnal/vertical mixing; $\partial(\omega c)$ is the difference between the vertical fluxes
170 through the top and bottom of each layer. The layer volume flux is diagnosed from the continuity
171 equation by

172 $$\partial(\omega) = -\left\{\nabla\cdot\boldsymbol{U} - \frac{\partial\Delta z}{\partial t}\right\} \qquad (2)$$

173 Daily-mean mass fluxes are used to compute the first term on the right-hand sides of (1) and
174 (2), whereas the change in the layer thickness (second term on the right-hand side of eq. 2) is
175 calculated from the instantaneous layer thicknesses. The conservation of mass is, therefore, exact
176 in the daily mean sense. $\mathfrak{D}(c)$ is calculated from daily-mean diffusivities saved in the online
177 simulation. A_h is the horizontal/isopycnal Laplacian diffusivity required for numerical stability;
178 its value is 0.01Δx in the control simulation, with Δx being the horizontal grid spacing. The
179 explicit diffusivity is significantly smaller than the eddy-induced diffusivity discussed in Section
180 3. Eq. 1 is solved using a three-dimensional, fourth-order advection scheme with flux-corrected
181 transport (Zalesak 1979). The time step is 1 hour. AOTM is forced with 5 years of data, which
182 are repeated every five years. To smooth a transition from the end of each 5-year cycle to the
183 beginning of the next one, blended values are used for all forcing fields for the first 16 days of

184 year 1. These blended values are calculated as a weighted average between first 16 days of year 1
185 and year 6.

186 To estimate the error due to the use of daily values in the offline calculations of the advective
187 and vertical-mixing terms, we carried out online and offline simulations of the same tracer. The
188 tracer is initialized to unity on the first day of year 4 in the region between longitudes 74.6W-
189 21.9W, latitudes 30.2N-36.8N and below the model layer 24; this layer depth varies between
190 approximately 300 and 1000 meters. At the end of year 4, these results are visually
191 indistinguishable from the offline simulations with AOTM simulations initialized in the same
192 way (Fig.1). We define the spatial standard deviation of a quantity g in a model layer as follows:

193

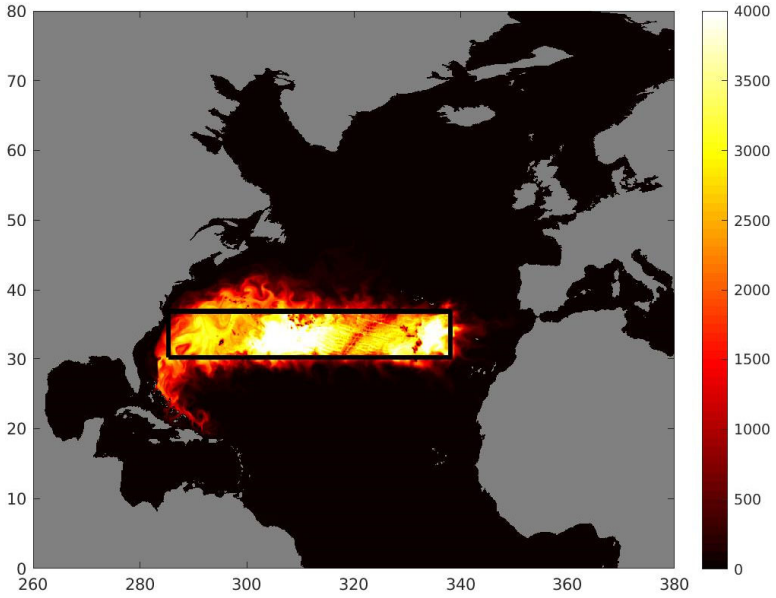

194

195 **Figure 1:** An idealized tracer used in the test of the offline approach, shown at the end of the
196 two-year integration. The black frame shows the initial distribution.

197 $$SD(g) = \left[\frac{1}{V}\int g^2 \Delta z \, dxdy - \left(\frac{1}{V}\int g \Delta z \, dxdy\right)^2\right]^{1/2} \quad (3)$$

198 where $V = \int \Delta z \, dxdy$ is the volume of the layer and g is smoothed by the running-mean 1° by 1°
199 filter (to remove grid-scale errors). A relative bias $e = SD(c_{offline} - c_{online})/SD(c_{online})$

remains between 2 and 9 percent in all layers. For the depth-integrated tracer values (tracer inventory), which will be the main variable discussed in this study, the errors are significantly smaller, with the relative bias e less than 0.6 per cent. Since even a small error in the position of the center of mass of a tracer patch could lead to large values of e, we also compared the tracer variance in both simulations. In the offline simulation, $SD(c_{offline})$ remains within 4 percent of the online value $SD(c_{online})$ in each layer below layer 24. Similar to Kamenkovich et al. 2017, we conclude that the errors due to the use of daily fields are sufficiently small to warrant the use of AOTM for simulations of passive tracers.

3 MESOSCALE VARIABILITY

The main goal of this study is to establish the important of mesoscale stirring in tracer distribution. We begin with the eddy-induced transport tensor $\boldsymbol{K}$ in the FULL_ADV simulation which will serve as a measure of eddy activity and its significance for tracer stirring and mixing. In the following part of the study, we will examine the importance of the eddy-induced advection by using separate experiments MEAN_ADV, in which the mesoscale variability is removed from the lateral volume fluxes and layer thickness.

Both approaches require a meaningful definition of the mesoscale. The definition is, however, not unique, because a clear scale separation between the mesoscale and seasonally varying large-scale fields does not exist. It is hard to design a method that would guarantee a complete removal of mesoscale processes from the 5 years of our model simulations. After a careful comparison of several approaches, we settled on a combination of time and spatial averaging: The data are first averaged in time and then smoothed spatially with a 25-by-25 point, moving area average filter, which is aligned with the latitude-longitude grid. Our analysis shows that this method removes the mesoscale variability more effectively than, for example, spatial smoothing alone, time averaging or smoothing in time. For example, our attempts to retain the climatological annual cycle by low-pass filtering all fields in time failed to remove a significant portion of mesoscale eddies, most notably, the Agulhas rings. Note that, although the spatial smoothing we use in this simulation broadens the Deep Western Boundary Current (DWBC) and reduces it peak speed, the DWBC volume transport is conserved.

The treatment of the diapycnal/vertical mixing in MEAN_ADV is even more challenging. Although the main focus of this study is on semi-adiabatic pathways below the surface mixed layer, the injection of the BIR tracer into these pathways depends on the vertical mixing in the upper ocean. Since the vertical diffusion within the mixed layer tends to be particularly strong in isolated regions of the North Atlantic, spatial or temporal smoothing would artificially increase these injection rates. To avoid this bias, we chose to use the full, unfiltered vertical/diapycnal mixing. We also tested two filtered values of the vertical diffusivity: (i) time-mean and spatially smooth diffusivity; (ii) diffusivity that is smoothed in time, but not in space. Although the main conclusions from these two tests remain the same as in our main MEAN_ADV simulation, these two settings resulted in a noticeably faster decline in the global BIR inventory.

3.1 Eddy diffusivity tensor

The calculation of the eddy transport tensor is based on the flux-gradient relationship between the lateral eddy-induced tracer flux $\boldsymbol{F_e}$ and the large-scale tracer gradient:

$$\overline{\boldsymbol{F_e}} = -\boldsymbol{K}\overline{\Delta z \boldsymbol{\nabla}\langle c\rangle} \tag{4}$$

where $\langle ... \rangle$ denote the 25-point running-mean 2D filter and the overbar stands for the 5-year average. The lateral direction is defined as horizontal in the surface mixed layer and isopycnal in the oceanic interior below it. The 2x2 transport tensor $\boldsymbol{K}$ is calculated in each model layer separately and stands for the lateral transport coefficient tensor; the tensor depends on location (i.e. is inhomogeneous) but is constant in time by definition. The methods used in this section are the same as in Kamenkovich et al. (2021) except that they used the time-dependent $\boldsymbol{F_e}$ in (4). The use of time-independent transport tensor here simplifies the discussion and reduces numerical errors, but ignores potentially important temporal fluctuations in the tensor.

The eddy flux $\boldsymbol{F_e}$ is the difference between the full flux and the flux due to the large-scale advection (used in MEAN_ADV):

$$\overline{\boldsymbol{F_e}} = \overline{\boldsymbol{U}c} - \overline{\langle \boldsymbol{U}\rangle \langle c\rangle}\ , \qquad \text{where } \boldsymbol{U'} = \boldsymbol{U} - \overline{\langle \boldsymbol{U}\rangle} \text{ and } c' = c - \overline{\langle c\rangle} \tag{5}$$

Note that in the isopycnal model layers, the large-scale layer thickness flux $\overline{\langle \boldsymbol{U} \rangle}$ includes the eddy-induced layer thickness fluxes, which represents the effects of eddies on density (Gent and McWilliams 1990). These fluxes are not discussed in this paper.

The flux-gradient relation (4) can be solved exactly for a given pair of tracers. Kamenkovich et al. (2021), however, found that in this case the tensor depends on the tracers used for the calculations; see also Bachman et al. (2020) and Sun et al. (2021) for the same conclusion. This tracer dependence makes the solution non-unique and casts doubts on applicability of the eddy diffusivity tensor, which is assumed to be tracer-independent in (4). A practical approach to this problem is to use multi-tracer ensemble-averaged estimates of eddy diffusivity (Abernathey et al. 2013; Bachman et al. 2020; Bachman et al. 2017). In this study, we follow the same logic and calculate the transport tensor in (4) as a least-square fit for four independent tracers, which are initially vertically uniform but have different horizontal profiles (see Appendix). Eighteen overlapping 110-day long simulations are carried out, with each consecutive segment starting 10 days before the end of the previous one; only the last 100 days of each simulation are used in the calculations.

Prior to solving (4), we remove the non-divergent ("rotational") flux component (Haigh et al. 2020; Jayne and Marotzke 2002; Marshall and Shutts 1981) which does not affect tracer distribution but tends to dominate $\boldsymbol{F_e}$. The rotational component is calculated for each tracer flux separately, using the Helmholtz decomposition (Lau and Wallace 1979):

$$\nabla \cdot \boldsymbol{F_e} = \nabla^2 \Phi, \;\; \nabla \times \boldsymbol{F_e} = \nabla^2 \Psi,$$

$$\boldsymbol{F_e} = \boldsymbol{F_{div}} + \boldsymbol{F_{rot}}, \tag{6}$$

$$\boldsymbol{F_{div}} = \nabla \Phi, \;\; \boldsymbol{F_{rot}} = \nabla \times \Psi.$$

In the above equations, Φ is the potential that corresponds to the divergent flux component $\boldsymbol{F_{div}}$, and Ψ is the streamfunction that corresponds to the rotational component $\boldsymbol{F_{rot}}$. The separation of $\boldsymbol{F_e}$ into the rotational and divergent components via the Helmholtz decomposition is, unfortunately, not unique and depends on the boundary conditions (Fox-Kemper et al. 2003; Jayne and Marotzke 2002; Maddison et al. 2015; Roberts and Marshall 2000), which are known for the total $\boldsymbol{F_e}$ but not for its rotational and divergent components, separately. The ambiguity in

boundary conditions leads to uncertainty in the transport tensor estimates (e.g. Kamenkovich et al. 2021). Because of the open boundaries in our domain, we chose to use the optimization technique with Tikhonov regularization (Li et al. 2006), which minimizes those components in $\boldsymbol{F}_{div}$ and $\boldsymbol{F}_{rot}$ that are both non-rotational and non-divergent; see Appendix. These opposing components cancel each other in $\boldsymbol{F}_{\boldsymbol{e}}$ but cause ambiguity in defining $\boldsymbol{F}_{div}$ and $\boldsymbol{F}_{rot}$ (Maddison et al. 2015). Note that for an exact solution of (4), the divergence of $\boldsymbol{F}_{div}$ and $\boldsymbol{F}_{\boldsymbol{e}}$ are the same $\nabla \cdot \boldsymbol{F}_{div} = \nabla \cdot \boldsymbol{F}_{\boldsymbol{e}}$ regardless of the boundary conditions used in the Helmholtz decomposition. The transport tensor $\boldsymbol{K}$ will, however, be sensitive to the particular definition of $\boldsymbol{F}_{div}$.

The transport tensor $\boldsymbol{K}$ can be separated into the symmetric and antisymmetric components, which have different physical meanings. The symmetric part, **S**, stands for a diffusive process affecting the tracer variance, while the antisymmetric component **A** represents advective effects. Note that the corresponding fluxes $\boldsymbol{S}\Delta z\boldsymbol{\nabla}\mathrm{c}$ and $\boldsymbol{A}\Delta z\boldsymbol{\nabla}\mathrm{c}$ will both have divergent and rotational components, unless the eddy-induced stirring is isotropic and homogeneous (Kamenkovich et al. 2021).

The diffusion tensor **S** can be further modified to show the preferred direction and efficiency of diffusion,

$$\mathbf{S} = \begin{bmatrix} S_{11} & S_{12} \\ S_{12} & S_{22} \end{bmatrix} = \mathbf{I}_R \begin{bmatrix} \lambda_1 & 0 \\ 0 & \lambda_2 \end{bmatrix} \mathbf{I}_R^T, \tag{7}$$

where $\mathbf{I}_R = \begin{bmatrix} \cos\theta & -\sin\theta \\ \sin\theta & \cos\theta \end{bmatrix}$ is a rotation matrix, θ defines the direction of the maximal diffusion and $\lambda_{1,2}$ are the corresponding eigenvalues (diffusivities). We define $\lambda_1$as the largest diffusivity and λ_2 – as the smallest diffusivity.

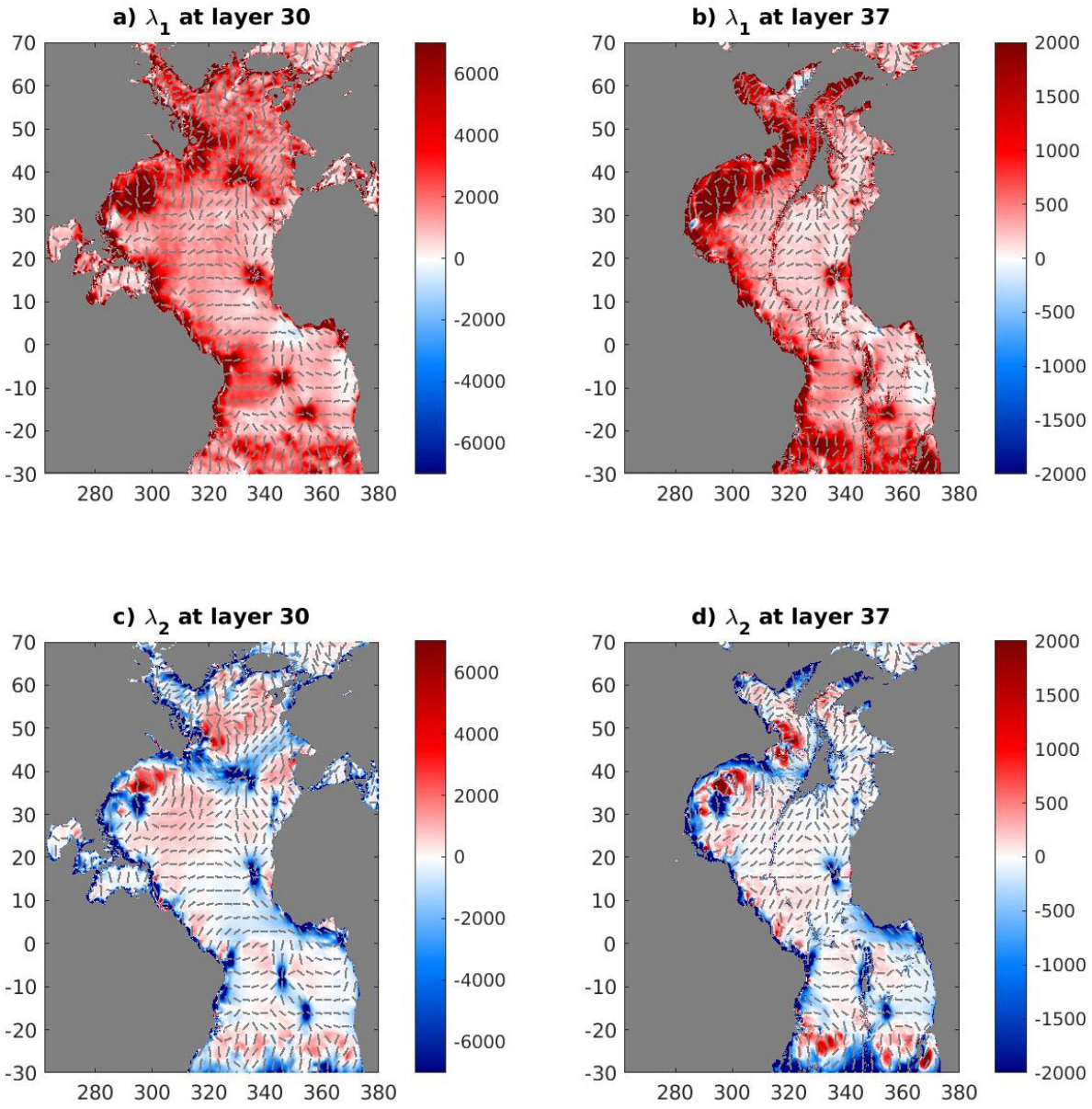

Figure 2: Eigenvalues of the diffusivity tensor **S**: λ_1 (largest, top row) and λ_2 (smallest, bottom row) eigenvalues of the diffusivity tensor (color shading) and the direction of the first eigenvector (lines, at every 40th point in each direction). Two model layers are shown: layer 30 (left column, zonal-mean depth of 388 m -1307 m) and layer 37 (right column, zonal-mean depth of 1,280 m - 3,430 m); the zonal average depths of these layers are also shown in Fig.5. Units are m^2s^{-1}.

Similar to the time-dependent diffusion tensor diagnosed from the same flow (Kamenkovich et al. 2021), the time-mean diffusion tensor in this study exhibits pairs of positive and negative eigenvalues, $\lambda_1 > 0$ and $\lambda_2 < 0$, in the oceanic interior (Fig. 2). This "polarity" results from eddies acting to bring tracer contours closer together in one direction while stretching the contours in the direction perpendicular to it (Haigh et al. 2021b; Sun et al. 2021). Although this eddy-induced filamentation can still correspond to net down-gradient transfer of variance (Haigh and Berloff 2021) or be balanced by large-scale advection in the full flow, negative λ_2 can lead to numerical instability if implemented in numerical models. In addition, the numerical stability is compromised by isolated extreme values in λ_1, resulting from weak tracer gradients $\boldsymbol{\nabla}\langle c \rangle$. For these two reasons, our attempts to use tensor **K** and its isotropic approximation in MEAN_ADV led to numerical instability and unphysical results. The investigation of the utility of representing eddies by the comprehensive tensor $\boldsymbol{K}$ is left for future studies with coarse-resolution models, and the analysis here is restricted to the description of the spatial inhomogeneity in the transport tensor.

Both eigenvalues decrease in magnitude with depth (Fig.2), which is expected, given the decrease in the eddy kinetic energy (not shown). The lateral variability is even stronger, and the magnitude of λ_1 changes by two orders of magnitude from the relatively quiet eastern part of the domain to very energetic western regions. Not surprisingly, the diffusivity is large around the path of the Gulf Stream and Deep Western Boundary Current. A particularly strong local maximum in the eddy-induced tracer stirring is found around approximately 35^{o}N in the deep western part of the domain, which will have important implications for the propagation of the BIR tracer from the north. Another region of elevated diffusivity λ_1 is the South Atlantic, which will be important for meridional spreading of the BIR tracer from the south boundary of the domain. Similarly strong spatial variations were reported in the previous estimates of the lateral diffusivity (e.g. Bachman et al. 2020; Haigh et al. 2020). Explanation of the origins of this variability is challenging because of the complexity of the flow and is beyond the scope of this paper, although large diffusivities can be expected in the regions where the isopycnals are steep, such as vicinity of the western boundary and Southern Ocean.

Another important characteristic of the diffusivity tensor $\boldsymbol{S}$ is the direction of the maximal eddy-induced dispersion (with the diffusivity λ_1), shown by the gray lines in Fig.2. This direction tends to be zonal in the oceanic interior between approximately 20S-30N, away from the coasts and major topographic features (Fig.2a). This predominantly zonal direction of the eddy-induced transport is consistent with previous Lagrangian estimates of the diffusivity tensor (Kamenkovich et al. 2015; Rypina et al. 2012). The direction of the maximal dispersion is, in contrast, nonzonal in most of the domain, especially north of 35N and south of 20S, near the "mixing hot spot" at 35^{o}N and in the vicinity of the western boundary (Fig. 2). In particular, deep layers tend to correspond to mostly nonzonal transport. The reported direction of the maximal dispersion will have two important implications for BIR distributions. Consistent with the idealized "leaky pipe" model, the eddies will spread the tracers zonally away from the western boundary, and these effects will be particularly important in the interior and far from topography. Secondly, the eddies will also facilitate meridional propagation of BIR tracers from both the north and south source regions, and these effects will be particularly important in the subpolar region, South Atlantic and near the western boundary.

The antisymmetric component **A** of the transport tensor corresponds to advective effects of eddies on tracers, with the streamfunction A_{12} and eddy-induced tracer velocities (EITV) $\boldsymbol{u_A} = (u_A, v_A)$:

$$\boldsymbol{A} = \begin{pmatrix} 0 & -A_{12} \\ A_{12} & 0 \end{pmatrix}, \quad u_A = -\frac{\partial A_{12}}{\partial y}, \qquad v_A = \frac{\partial A_{12}}{\partial x} \tag{8}$$

EITV multiplied by the large scale layer thickness $\overline{\langle \Delta z \rangle}$ are shown in Fig.3, together with the large-scale layer volume fluxes $\overline{\langle \boldsymbol{U} \rangle}$. EITV are smaller in magnitude than $\overline{\langle \boldsymbol{U} \rangle}$ in most of the domain, except the mixing hotspot near 35N and western boundary region. In the latter locations, v_A tends to be southward, which means that eddies will facilitate southward spread of BIR tracers in the deep layers. Note that EITV and $\overline{\langle \boldsymbol{U} \rangle}$ have different physical meaning and properties. $\overline{\langle \boldsymbol{U} \rangle}$ represents the the actual large-scale transport of water within each layer, both due to the large-scale velocities and eddies; divergence of this transport leads to changes in the layer thickness and generate diapycnal exchanges. In contrast, EITV describe the advective part of the tracer transport, do not affect density and are non-divergent (e.g. Haigh et al. 2021a). The relative

importance of the advective (tensor **A**) and diffusive (tensor **S**) processes depends on the large-scale tracer structure. For example, consider a highly idealized case of a linear tracer profile with constant $\boldsymbol{\nabla}\langle c\rangle$. Since all second derivatives in $\langle c\rangle$ are zero, the advective transport by EITV can be expected to dominate the tracer distribution.

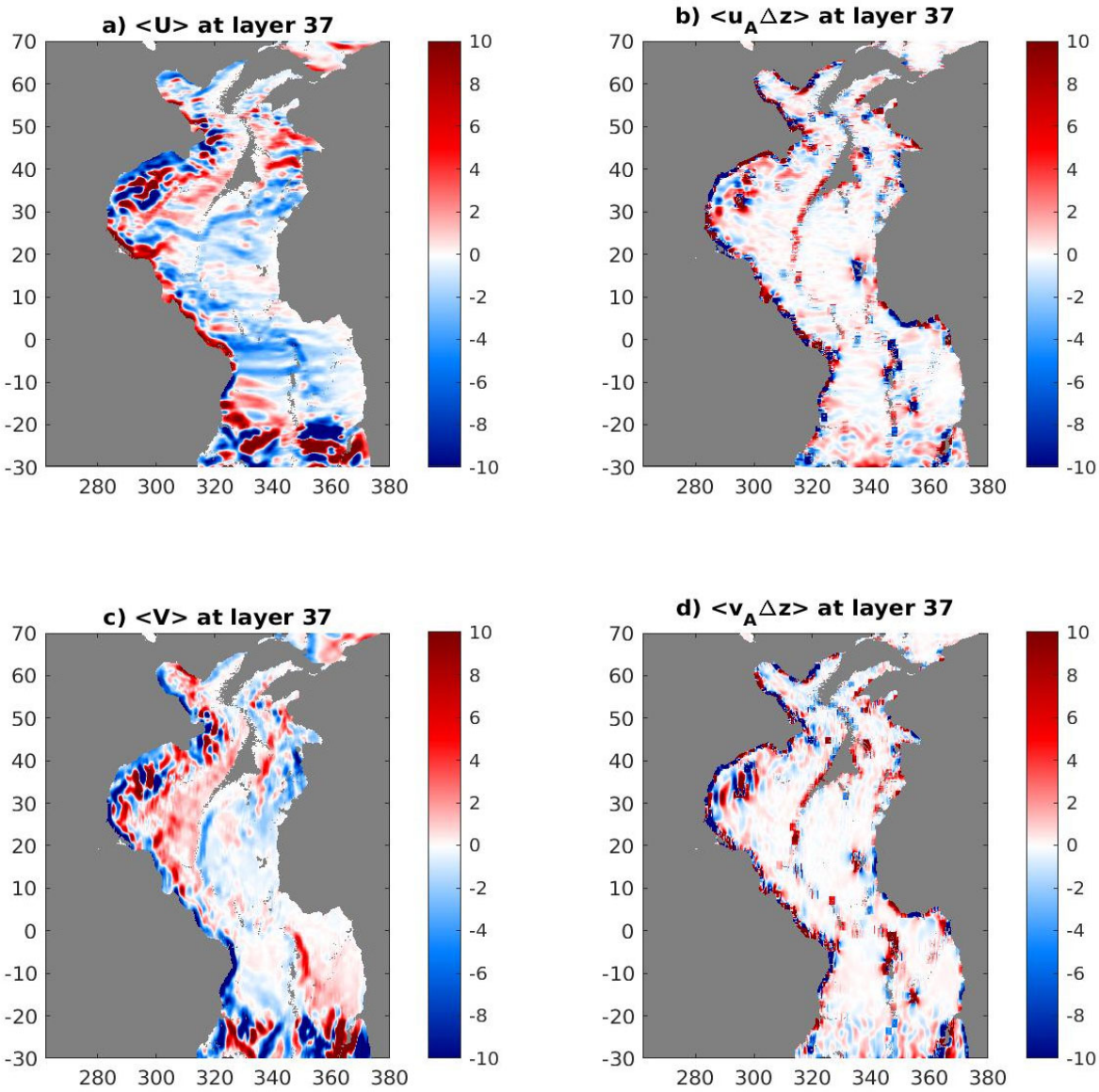

Figure 3: Large-scale layer volume flux $\langle\overline{\boldsymbol{U}}\rangle$ and EITV multiplied by the large scale layer thickness $\langle\overline{\Delta z}\rangle$ at layer 37 (zonal-mean depth of 1,280 m - 3,430 m): a) zonal flux $\langle U\rangle$; b) eddy induced zonal velocity times layer thickness $\langle u_A\overline{\langle\Delta z\rangle}\rangle$; c) meridional flux $\langle V\rangle$; b) eddy induced meridional velocity times layer thickness $\langle v_A\overline{\langle\Delta z\rangle}\rangle$. Units are m^2s^{-1}.

4 SIMULATIONS OF THE BIR TRACERS

In this study we consider two BIR tracers, one originating from the surface area in the North Atlantic (north of 50ºN, NBIR hereafter), and another coming from the southern lateral boundary of the domain (at 30ºS, SBIR hereafter). These BIR tracers correspond to propagation of pulses from the corresponding boundaries, but do not constitute a complete set of Green functions. During year 1, NBIR is set to unity at the surface north of 50ºN and to zero south of this latitude; starting at year 2, the tracer is set to zero over the entire surface boundary. Similarly, SBIR is set to unity at the southern boundary of the model domain during year 1 and to zero starting at year 2. Surface fluxes of SBIR are always zero. There are no other sources and sinks in the rest of the domain. Both tracers are nondimensional. We carried out only one simulation for each tracer and use it to describe the propagation of a boundary forced signal within AMOC.

4.1 NBIR simulations

During the first year, when the NBIR tracer is set to unity at the surface north of 50ºN, the tracer quickly fills the mixed layer and begins spreading into the rest of the domain. As the tracer is being removed from the surface starting at year 2, the total tracer inventory begins to decline while the tracer also spreads around the entire domain. The decrease in the inventory is fast initially, but then slows down as less and less tracer-rich waters come in contact with the surface. If we neglect tracer exchanges with regions outside of the model domain, the change in the total tracer inventory will be determined by the tracer loss from the surface. The tracer removal rate from the surface can be assumed to be proportional to the tracer concentrations c_{ML} within the surface mixed layer,

$$\frac{\partial}{\partial t}\iiint c dV \approx -\alpha \iint c_{ML}\, dS, \tag{8}$$

The parameter α in the above relation is the removal speed that depends on how fast the tracer within the mixed layer is re-supplied to the surface due to vertical mixing and advection. In the limit of very strong vertical mixing, the tracer is instantly homogenized within the mixed layer and $\alpha = {}^{\Delta z}/_{\Delta t}$, where Δz is the thickness of the topmost model layer (1 m) Δt is the time step (1 hour). In the absence of lateral advection and stirring, the tracer stays within the mixed layer and $c = c_{ML}$. Assuming that the mixed layer has a uniform thickness of h=300 m, the tracer

concentration is then decaying exponentially with an e-folding time of $\Delta t\, {}^{h}/_{\Delta z}$=O(10 days). The tracer response in this case is indeed a short-lived pulse that quickly dissipates with time. The advection decreases c_{ML} reducing the removal rate, the right-hand side of (8). The resulting decline in the total inventory is significantly slower than in the case with no advection and is different from exponential. For example, the time scale $T_r = \iiint c dV \left\{-\frac{\partial}{\partial t}\iiint c dV\right\}^{-1}$, which would be an e-folding time scale ${}^{1}/_{\alpha}$ if the decay were purely exponential, changes from approximately 2.5 years to almost 34 years from year 1 to year 25 for FULL_ADV. The decay time scale T_r is also very sensitive to the lateral advection. In MEAN_ADV, the lack of eddy-induced stirring increases the surface removal rate and the parameter T_r is shorter than in FULL_ADV, varying from 2 years to approximately 22 years. As the result, the total inventory of NBIR in MEAN_ADV is noticeably smaller than in FULL_ADV, with the ratio between two inventories being as large as almost 4.0 by the end of the 100-year simulation.

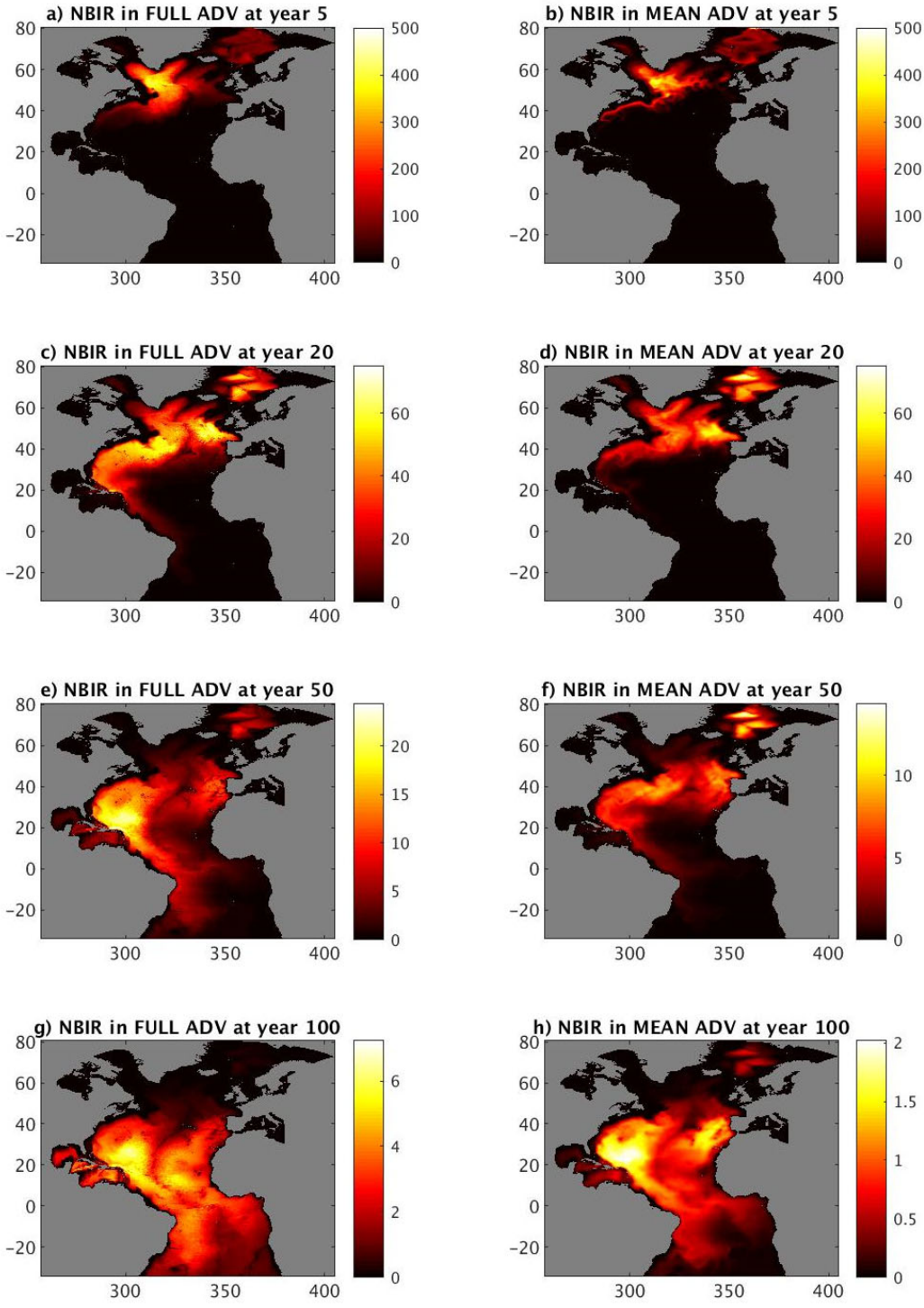

415

416 **Figure 4:** Annual-mean inventory (vertical integral) of the NBIR tracer in FULL_ADV (left
417 column) and MEAN_ADV (right column). Note different color scales in panels. The tracers are
418 nondimensional and the units of the inventory are meters.

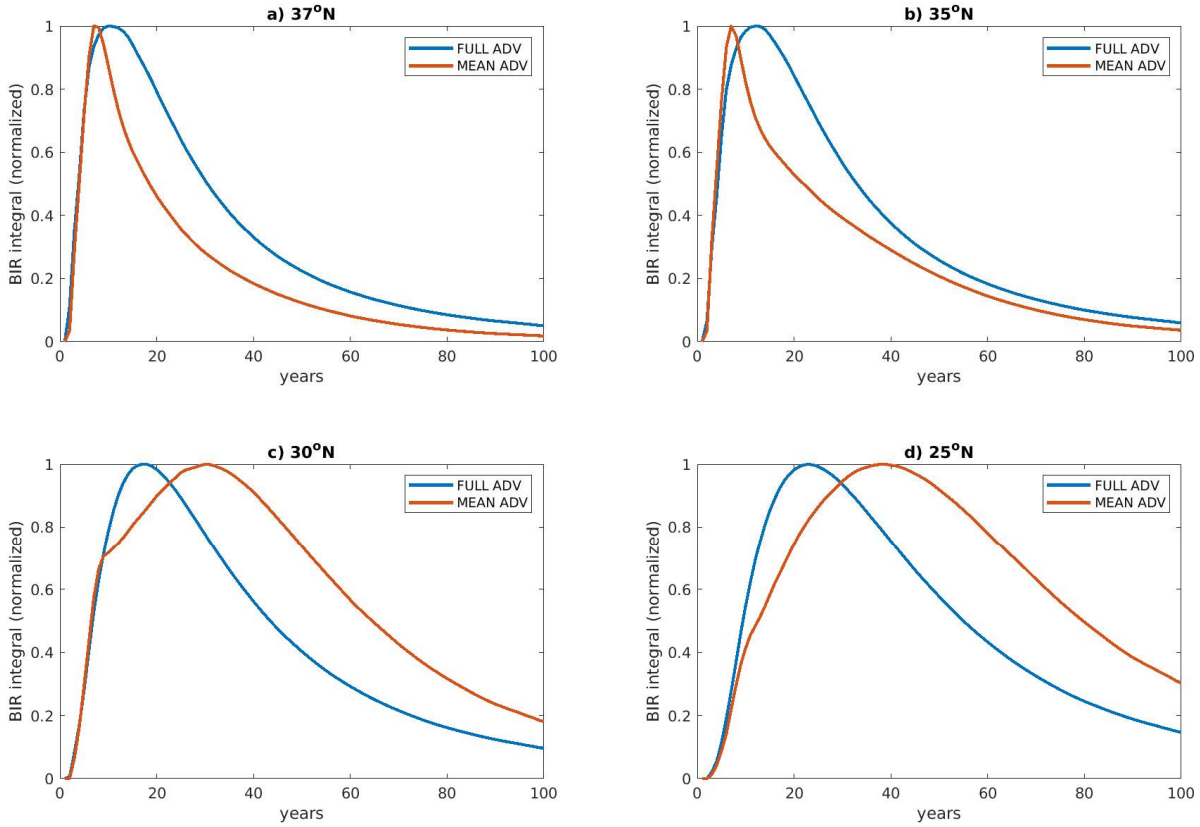

Figure 5: Annual-mean zonal integrals of NBIR inventories at four different latitudes as functions of time. The integrals are calculated over 200 grid points (15.9 degrees longitude) from the western boundary. For presentation purposes, each curve is divided by its maximum and smoothed in time by a 5-point running-mean filter.

With time, the BIR pulse in both simulations leaves the mixed layer in the high latitudes and propagates southward within the WBC (Fig. 4a-b). The horizontal distribution and associated timescales are, however, different between the two runs. The tracer is subject to lateral mixing by mesoscale eddies in the FULL_ADV simulation, which removes the BIR tracer from the mean pathway and spreads it into the interior (Maltrud et al. 2010; Waugh and Hall 2005). The eddy-induced diffusivities (Fig.2) indeed show predominantly zonal downgradient tracer transport in large parts of the mid- and low-latitude interior. According to an idealized "leaky pipe" model in Waugh and Hall (2005), the zonal exchange between the WBC and the deep interior broadens the BIR pulse and slows its southward propagation. How different is AMOC in our study from the idealized leaky-pipe solution?

Propagation of the pulse in the FULL_ADV case is indeed slower than in MEAN_ADV north of the Gulf Stream. For example, the NBIR pulse arrives at the Cape Hatteras (35ºN) during year 6 in MEAN_ADV (Fig.5a), which implies a propagation speed of approximately 0.01 m s^{-1}, whereas the NBIR peak in the FULL_ADV case arrives at this latitude later, during year 10. For comparison, the speed of DWBC in MEAN_ADV is between 0.02-0.05 ms^{-1}, and peak speeds are even faster in FULL_ADV. According to the leaky-pipe model, the difference between the WBC and NBIR propagation speeds can be explained by lateral tracer spreading in the vicinity of the western boundary, which is driven by the eddy-induced mixing in FULL_ADV and large-scale recirculation in FULL_ADV and MEAN_ADV. The peak passage is also more spread out in time in FULL_ADV (Fig.5a-b), which is qualitatively consistent with the analytical TTD derived for the leaky-pipe model (Waugh and Hall 2005).

After reaching the Cape Hatteras, the southward propagation of the tracer pulse slows down in both simulations (Fig.4a-b), which is possibly explained by the interaction of the DWBC with the northeastward flowing Gulf Stream. At the same time, this region is a "hot spot" of eddy-induced mixing, according to our analysis of the eddy diffusion and advective tensors (Figs.2 and 3), since both tensors exhibit large meridional spreading in this region. The eddies thus facilitate propagation of the NBIR pulse southward of 35ºN in FULL_ADV, and their absence explains a much slower propagation of the pulse in MEAN_ADV. As a result, the NBIR pulse arrives at 25ºN during year 22 in FULL_ADV and only during year 40 in MEAN_ADV (Fig.5c-d). On later stages, the tracer fills the Abyssal Plain, and the region corresponds to a local maximum in the BIR inventory in both simulations (Figs.4g-h).

The spreading of the NBIR tracer to the east of the mid-Atlantic ridge is slower than in the west and the difference between FULL_ADV and MEAN_ADV simulations is less pronounced there (Fig.4e-h). At the depths shallower than the top of the ridge, the tracer is advected eastward from the western Atlantic within multiple zonal jets (Fig.3a; Kamenkovich et al. 2009; Maximenko et al. 2008) and by mesoscale eddies (Figs.2 and 3). The signature of the jet advection is mostly observed in MEAN_ADV in the model layers 1 to 34, which correspond to the average depth of approximately 1900-2200 m (not shown), but is also visible in Figs.4c-f. The eddy-induced transport is also predominantly zonal at these depths, south of approximately

30ºN (Fig.2a). Other pathways include the eastward deep Equatorial current (Fig.4e-f). In the deeper layers, eastward propagation of the tracer is impeded by the mid-Atlantic Ridge, although the tracer can still get through multiple fracture zones. Once the tracer ends up in the eastern part of the basin, it slowly spreads southward, forming a secondary pulse. This secondary pulse in FULL_ADV moves noticeably faster than in MEAN_ADV and reaches the Tropics by year 100, whereas the eastern pulse stays north of approximately 25ºN in MEAN_ADV. The NBIR distribution south of the Equator by year 100 are qualitatively similar between the FULL_ADV and MEAN_ADV simulations (Fig. 4g-h).

The broad NBIR pulse in the FULL_ADV case extends farther south than in MEAN_ADV at most depth levels, as is evident in the depth-latitude (zonally integrated) plots (Fig.6). The difference becomes particularly large by year 100, when 30 per cent of the total NBIR inventory is found south of the Equator in FULL_ADV, compared to only 17 per cent in MEAN_ADV. These depth-latitude plots also exhibit a two-layer structure of the NBIR pulse. The position of the maximum in NBIR concentrations below the 2000-m depth is similar between the two cases, does not change with time and is associated with the deep Abyssal Plain. The difference between the two simulations is most pronounced near the 2000 m depth (layer 34): The FULL_ADV simulation exhibits a strong NBIR pulse near approximately 15ºN, whereas the MEAN_ADV pulse is much weaker and is located farther north.

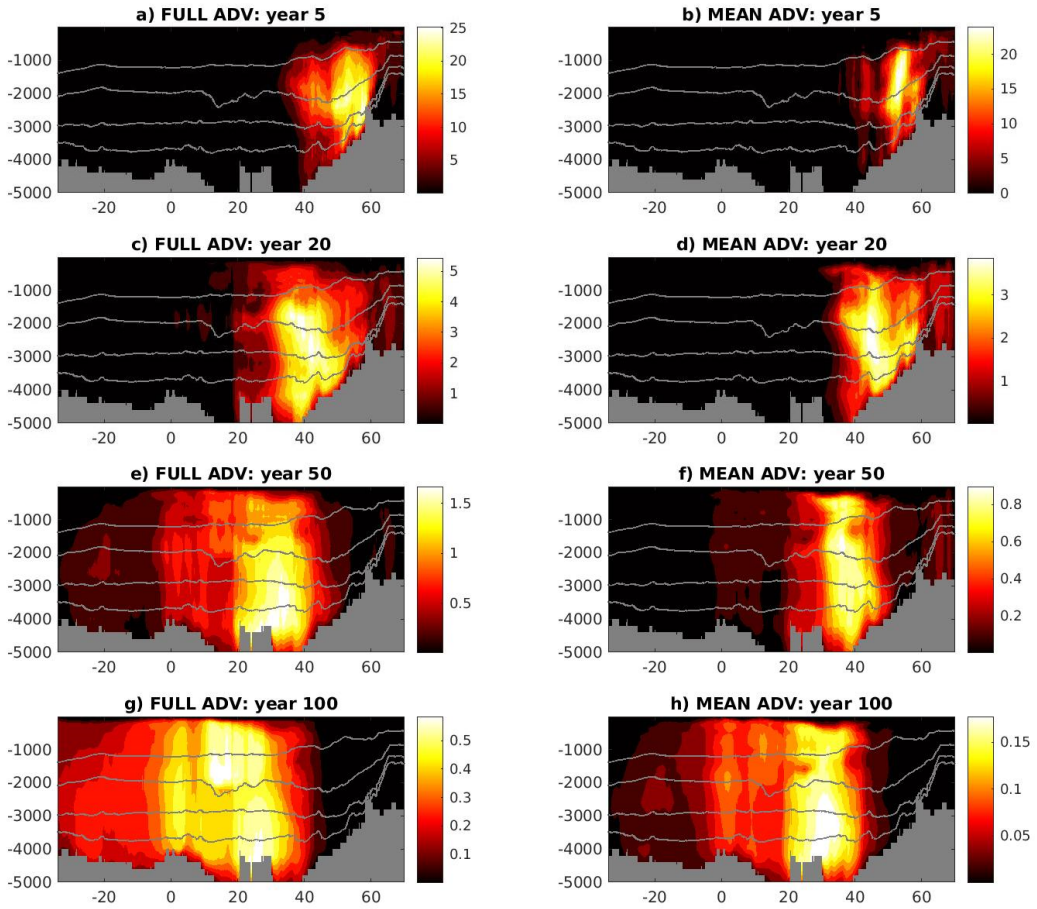

Figure 6: Annual-mean zonal integral of the NBIR concentrations on the latitude-depth plane in FULL_ADV (left column) and MEAN_ADV (right column). The tracer concentration is first integrated in the zonal direction and within each layer and then interpolated to z-coordinates using zonal mean layer depth. The lines show the mid-depth of model layers 30, 34, 36 and 37, zonally and time averaged. Note differences in the color contour intervals; units are 10^4 m.

4.2 Southern BIR tracer

Using the same concept as NBIR, the SBIR tracer quantifies the advective timescales and pathways of the signal propagation from the Southern Ocean into the Atlantic. Similar to the NBIR tracer, the SBIR pulse separates from the boundary, where it is being removed beginning at year 2, and moves with AMOC currents. The total SBIR inventory is, however, significantly less sensitive to the presence of mesoscale eddies, and the difference between the FULL_ADV and MEAN_ADV inventories at year 50 is only 17 per cent. The main SBIR pathways are

associated with the northward spread of the Antarctic Intermediate water (AAIW) in the southwestern Atlantic, the Agulhas leakage in the southeastern Atlantic and the propagation of the Antarctic Bottom Water (AABW) in the deepest layers. In our discussion, we will, therefore, distinguish between the upper 2000 m (layers 1-34) and deep layers below. Most of the SBIR tracer is found in the deep layers by the end of simulations: 53 percent in FULL_ADV and 56 percent in MEAN_ADV.

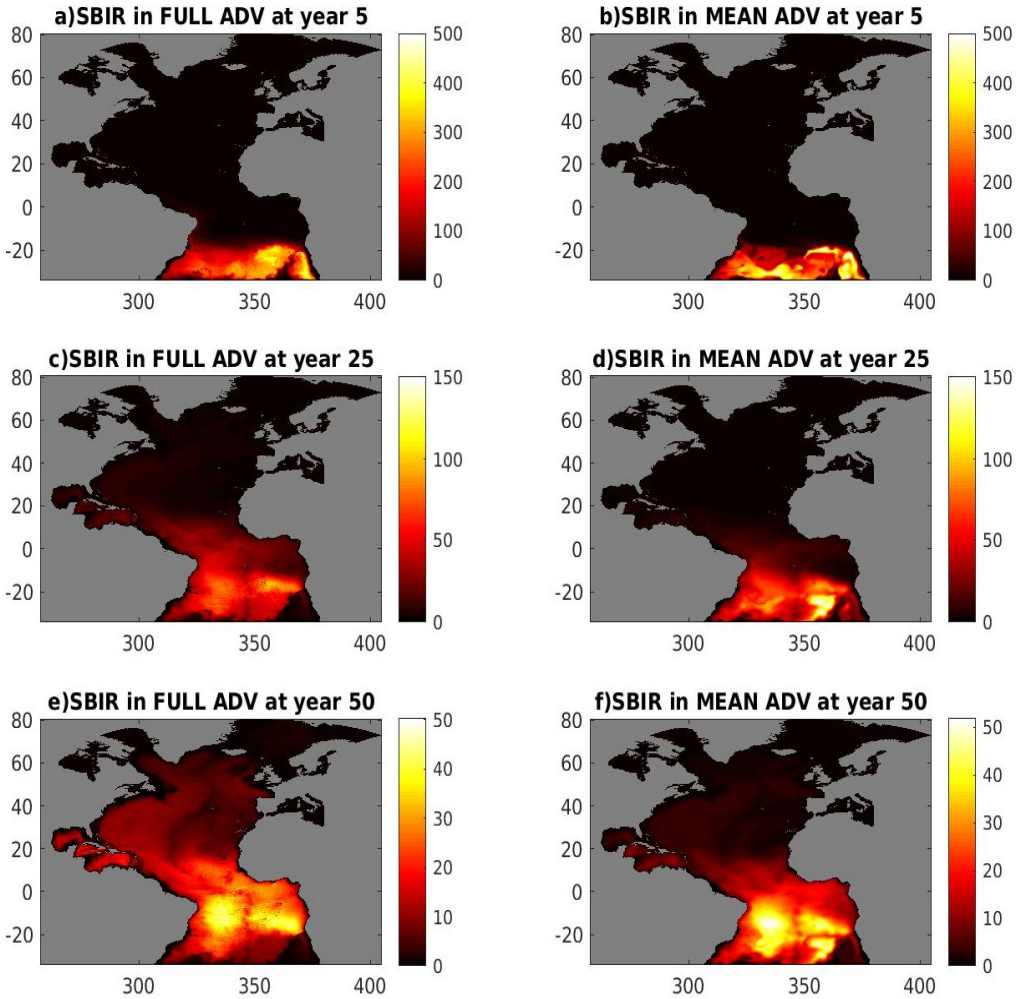

Figure 7: Annual-mean inventory (vertical integral) of the SBIR tracer in FULL_ADV (left column) and MEAN_ADV (right column). Note different color scales in panels. The tracers are nondimensional and the units of the inventory is meters.

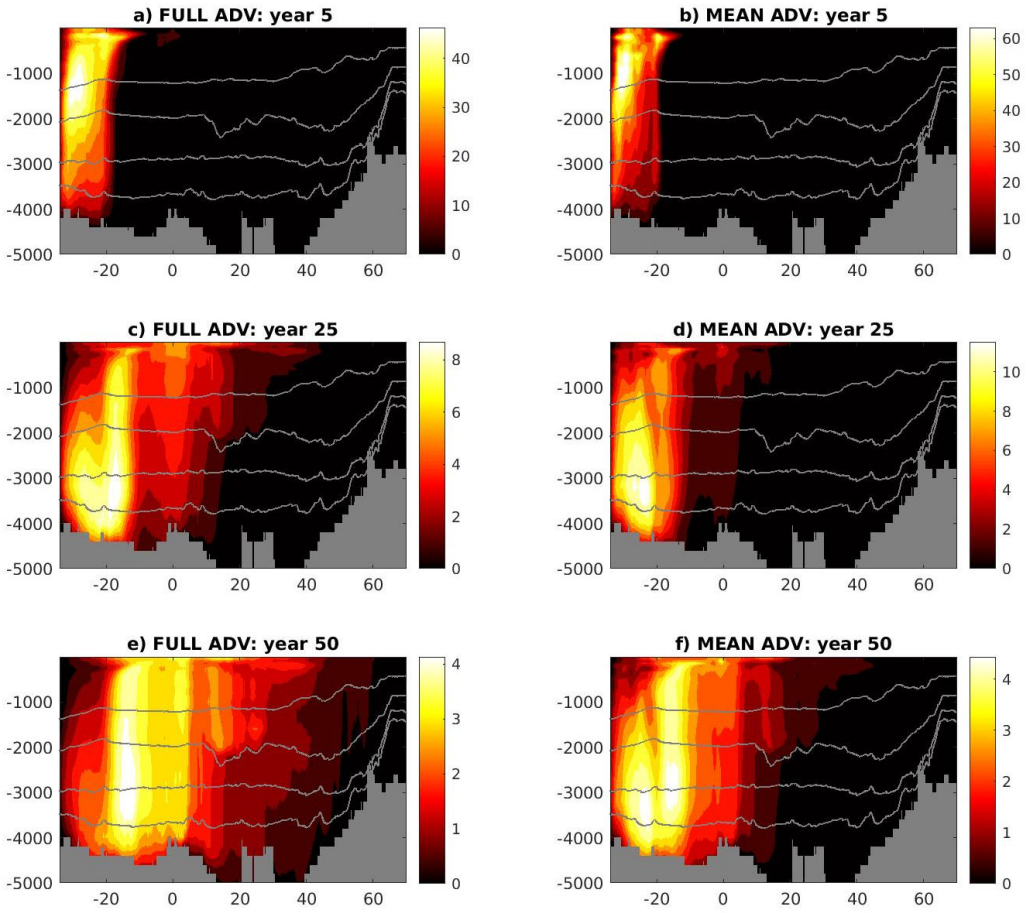

506

507 **Figure 8:** Annual-mean zonal integral of the SBIR concentrations on the latitude-depth plane in
508 FULL_ADV (left column) and MEAN_ADV (right column). The tracer concentration is first
509 integrated in the zonal direction and within each layer and then interpolated to z-coordinates
510 using the zonal mean layer depth. The lines show the mid-depth of model layers 30, 34, 36 and
511 37, zonally and time averaged. Note differences in the color contour intervals; units are 10^4 m.

512 Propagation of the SBIR tracer in the deep layers is steered by major topographic features:
513 the mid-Atlantic ridge, the Rio Grande Rise in the west, and the Walvis Ridge in the east. The
514 SBIR tracer first enters the Atlantic domain in the southeast. The tracer initially fills the region
515 south of the Walvis Ridge (Fig.7a,b), within the eastern boundary, but is gradually transported
516 out of the Atlantic due to the continuing water exchange with the Southern Ocean. These
517 exchanges are facilitated in FULL_ADV by eddy-induced diffusive fluxes, which are nearly
518 meridional in the southernmost part of the model domain (Fig.2) and which explain smaller
519 inventories of SBIR compared to MEAN_ADV. Starting at approximately year 10, we observe

two deep pulses moving northward, one to the west and another to the east of the mid-Atlantic ridge. Assisted by the eddy-induced stirring, these deep tracer pulses propagate faster in FULL_ADV than in MEAN_ADV, although the overall difference is less pronounced than in the case of NBIR (Fig. 7c-f). Despite relatively large magnitudes of the eddy diffusivity in the South Atlantic, the direction of the eddy-induced stirring is primarily zonal north of 20ºS (Fig.2) and the position of the center of these deep tracer pulses is similar between the two simulations.

The SBIR tracer pulse is more spread out meridionally in the FULL_ADV simulation. By the end of the simulation, 40 percent of the tracer is found in the Northern Hemisphere, compared to only 20 percent in MEAN_ADV. The tracer moves faster in the upper layers, and the northward extent of the SBIR pulse is significantly larger in the upper 2000 meters (Fig.8). By the end of the FULL_ADV simulation, most of the tracer (58 percent) is found in the Northern Hemisphere. The distribution is more uniform vertically in MEAN_ADV, with 36 percent of the tracer found north of the Equator.

5 DISCUSSION AND CONCLUSIONS

Redistribution of tracer anomalies takes place along AMOC pathways that link the high-latitude North Atlantic with the mid-latitudes and the Southern Ocean. Within the most basic schematic of a semi-adabatic AMOC, these tracer anomalies enter and leave the Atlantic Ocean from the surface in the northern high latitudes and through lateral exchanges with the Southern Ocean. The “conveyor belt” concept, however, hides underlying complexity of a three-dimensional system of currents on a wide range of spatial scales. Our numerical study evaluates the importance of mesoscale currents (“eddies”) in these AMOC pathways and associated timescales. The contribution of eddies remains poorly understood, mainly because of challenges in studying these effects over large distances and long times. The offline tracer model used in this study overcomes this technical difficulty because it permits extended simulations at the relatively low computational cost. More important for the study is, however, the unique ability of offline simulations to isolate the direct contribution of eddies to the large-scale distribution of oceanic tracers. This task is achieved by a sensitivity run with a synthetic time-averaged and spatially smoothed currents. The study considers two Boundary Impulse Response (BIR) tracers, which can be used to quantify the importance of the Atlantic tracer exchanges with the high-

549 latitude atmosphere in the north and with the Southern Ocean in the south. The results are
550 interpreted using eddy-induced transport tensors, which are derived from lateral distributions of a
551 separate set of idealized tracers.

552 The results provide several examples of the importance of eddies in propagation of BIR
553 tracers. During the early stages of the simulation, eddy advection allows for more tracer to
554 remain in the ocean and, thus, increases the overall BIR inventory. This effect can be interpreted
555 as the eddy-induced enhancement of the overall ventilation. Specifically, eddies facilitate the
556 removal of BIR away from the North Atlantic surface, where the waters are being continuously
557 renewed and BIR tracer concentrations are being depleted by the atmosphere. It is not, however,
558 easy to quantify this potentially important effect of eddies in our study. The stratification in the
559 sensitivity simulation MEAN_ADV is different from the control run FULL_ADV and it would
560 be difficult to claim that the difference in tracer inventories observed here is due solely to
561 mesoscale advection, despite the same vertical diffusivities in both simulations. In addition, at
562 time scales longer that those considered in this study, the eddy-induced mixing can be expected
563 to expose more tracer to the surface and thus facilitate tracer removal.

564 In agreement with an idealized leaky-pipe model, the eddies spread the tracer away from the
565 main DWBC pathway, which increases the advective timescale within AMOC at the early
566 stages. Zonal eddy-induced transports move the tracer over the mid-Atlantic Ridge to the eastern
567 part of the domain, which helps to achieve a more spatially uniform ventilation of the Atlantic
568 interior. The eddy effects are not, however, limited to the eastward spreading of the tracer from
569 the western boundary. The mesoscale currents also facilitate the meridional spreading of the
570 NBIR tracer south of the eastward Gulf Stream extension and across the deep Equatorial current
571 farther south. In this sense, the eddies assist the large-scale advection, and the resulting
572 meridional propagation of the NBIR pulse is noticeably faster in the presence of mesoscale
573 currents. Similarly, the meridional propagation of the SBIR tracer from the southern boundary of
574 the Atlantic is also facilitated by mesoscale eddies.

575 The results also demonstrate the importance of spatial inhomogeneity and anisotropy of
576 eddy-induced mixing, demonstrated by the eddy-induced diffusion and advection tensors. The
577 anisotropy of the eddy diffusivity and the direction of the maximal eddy-induced dispersion are

clearly important for the propagation of tracers within AMOC. For example, the eddy-induced stirring is primarily zonal in the mid- and low-latitude interior, far from the coasts and topographic features. Zonal mixing is also very strong in the South Atlantic (north of 20ºS), and the resulting re-distribution of temperature and salinity anomalies will help to establish a basin-wide west-east density contrast, which is particularly important for the AMOC dynamics (Kamenkovich and Radko 2011). Nevertheless, the eddy-induced diffusion and advection have significant meridional components near the western boundary and in deep ocean layers, which assists the meridional propagation of the pulse. For example, a mixing "hot spot" in the vicinity of the eastward Gulf Stream extension helps to move the NBIR pulse southward of this location. An accurate calculation of the transport tensors is, however, challenging, due to uncertainty in tracer-based estimates of the eddy diffusivity revelealed by previous studies (e.g., Bachman et al. 2020; Kamenkovich et al. 2021; Sun et al. 2021) and should be interpreted with caution.

Eddy-induced diffusivities and the corresponding tracer transports are complex, but the significance of this complexity for large-scale tracer distirbutions remains unclear. This study combines an analysis of eddy-induced transport tensor and a direct inquiry into the importance of eddy-induced advection for tracer distribution. The time-independent transport tensor discussed in this study still lacks important temporal fluctuations (Haigh et al. 2020; Kamenkovich et al. 2021). The attempts to use the diagnosed eddy-induced diffusivities in place of eddies in our study was, however, unsuccessful due to numerical instability. The instability was most likely caused by negative and large positive values of diffusivity and the presence of sharp gradients in high-resolution simulations. An alternative approach of using coarse-resolution simulations with parameterized tracer transports would involve different large-scale circulation, leading to additional challenges with interpretation.

Most notable challenge in any analysis of mesoscale dynamics is the lack of a clear scale separation between the large-scale AMOC and mesoscale currents. Time-based definitions of mesoscale variability complicate its separation from the seasonal cycle in the large-scale fields, and the simple 5-year time average used in this study assumes that seasonal anomalies in AMOC are weaker than the mesoscale currents. On the other hand, definitions based on a spatial scale, also used in this study, result in additional eddy-induced terms in the tracer budgets (e.g. Sun et

al. 2021). At the same time, a spatial scale-based approach seems as a natural way to define mesoscale anomalies missing in coarse-resolution ocean models.

This study focuses on the direct contribution of eddy-induced tracer fluxes, by assuming that the large-scale circulation is the same in both simulations. The important effects of eddies on large-scale currents are, therefore, outside the scope of this study. For example, the eddies have been shown to play a key role in the dynamics of western boundary currents and their eastward extensions (e.g., Shevchenko and Berloff 2015; Waterman et al. 2011) and mid-latitude stratification (Henning and Vallis 2004). In addition, eddy-induced zonal jets (Kamenkovich et al. 2009; Maximenko et al. 2008) are shown to be important for spreading of the ventilation signal to the eastern part of the deep Atlantic. The absence of these eddy-driven currents in coarse-resolution models will, therefore, further increase their biases in tracer distributions. Finally, mesoscale and submesoscale currents can also be expected to play a role in the variability of the mixed-layer depth which has been shown to modulate the air-sea heat exchanges (Tozuka and Cronin 2014; Gao et al. 2021, in press), and submesoscale currents, which are missing in our study, can be particularly important for ventilation (Callies et al. 2015). Studies of the importance of eddy-induced advection for tracer distirbution should clearly be continued, as they are needed for evaluation of eddy-permitting simulations, that stop short of full resolution of mesoscale, as well as for development of eddy parameterization schemes.

Acknowledgements This study was supported by NOAA's Climate Program Office, Climate Variability and Predictability Program (award NA16OAR4310165). Kamenkovich also acknowledges the support of the National Science Foundation (grant 1849990) and high-performance computing support from Cheyenne (doi:10.5065/D6RX99HX) provided by NCAR's Computational and Information Systems Laboratory, sponsored by the National Science Foundation.

633 **Data Availability Statement** Data used for the main analysis and figures in the paper will be
634 openly available from a public repository. Complete data from numerical simulations will be
635 made available upon request. There are no restrictions on the data use.

636

637 **APPENDIX A**

638 Eighteen overlapping 110-day long simulations are carried out, with each consecutive
639 segment starting 10 days before the end of the previous one. Four idealized conservative tracers
640 were initialized with the following analytical horizontal profiles:

641
$$c_1 = 1 - \frac{n_x}{N_x}, \quad c_2 = 1 - \frac{n_y}{N_y}$$
$$c_3 = \left(\frac{n_x - N_x/2}{N_x/2}\right)^2 + \left(\frac{n_y - N_y/2}{N_y/2}\right)^2, \quad c_4 = \cos\left(\frac{\pi n_x}{720}\right)\cos\left(\frac{\pi n_y}{720}\right) \tag{A1}$$

642 where $n_x = 1, \dots, N_x$ and $n_y = 1, \dots, N_y$ are grid indices in the zonal and meridional directions
643 and $N_x = 1475$ and $N_y = 1950$ are the total number of grid points in each corresponding
644 direction. Each of these profiles is multiplied by the following "hat function" $h(n_y)$, in order to
645 minimize the effects of the open boundaries:

646
$$h(n_y) = \begin{cases} exp\left[-\left(\frac{n_y - 925}{700}\right)^6\right], & 50 < n_y < 1800 \\ 0, & \text{otherwise} \end{cases} \tag{A2}$$

647 The initial tracer concentrations (A1)-(A2) are uniform vertically. The tracers do not have
648 internal sources and sinks, and their surface fluxes are zero.

649 We use the optimization technique with Tikhonov regularization (Li et al. 2006) to extract
650 the divergent component in eddy fluxes. The method minimizes the opposing non-rotational and
651 non-divergent components in $\boldsymbol{F}_{div}$ and $(\boldsymbol{F}_{\boldsymbol{e}} - \boldsymbol{F}_{div})$. These components cancel each other in the
652 sum $\boldsymbol{F}_{\boldsymbol{e}}$ but cause ambiguity in defining $\boldsymbol{F}_{div}$ and $\boldsymbol{F}_{rot}$.The main advantage of this method for
653 our study is that it avoids the need for boundary conditions, which are particularly ambiguous at
654 the open boundaries. Note that the decomposition preserves boundary conditions for $\boldsymbol{F}_{\boldsymbol{e}}$.

655 The finite-difference form of the equation (6) is first written in the following matrix form

$$\boldsymbol{y} = \boldsymbol{A}\boldsymbol{x}, \qquad \text{where} \quad \boldsymbol{y} = \begin{pmatrix} F_x \\ F_y \end{pmatrix} \text{ and } \boldsymbol{x} = \begin{pmatrix} \Phi \\ \Psi \end{pmatrix} \tag{A3}$$

The solution for $\boldsymbol{y}$ is then obtained by minimizing the objective functional

$$J_\alpha(\boldsymbol{x}) = \frac{1}{2}(\boldsymbol{y} - \boldsymbol{A}\boldsymbol{x})^T(\boldsymbol{y} - \boldsymbol{A}\boldsymbol{x}) + \alpha\frac{1}{2}\boldsymbol{x}^T\boldsymbol{x} \tag{A4}$$

where "T" stands for the transpose, and the regularization parameter $\alpha = 10^{-15}\, m^{-2}$. Minimization of the regularization term (second term on the right-hand side) is equivalent to minimizing the opposing irrotational, nondivergent components of flux that cause uncertainty in the decomposition (Li et al. 2006). We use the quasi-Newton method with limited memory Broydon – Fletcher – Goldfarb – Shanno (BFGS) updating (a bulti-in Matlab function). The equation (4) is solved locally by matrix division function in Matlab, which determines the solution in the least square sense to the overdetermined system of equation.

REFERENCES

Abernathey, R., and J. Marshall, 2013: Global surface eddy diffusivities derived from satellite altimetry. *J Geophys Res-Oceans*, **118,** 901-916.

Abernathey, R., D. Ferreira, and A. Klocker, 2013: Diagnostics of isopycnal mixing in a circumpolar channel. *Ocean Model*, **72,** 1-16.

Bachman, S. D., B. Fox-Kemper, and F. O. Bryan, 2020: A Diagnosis of Anisotropic Eddy Diffusion From a High-Resolution Global Ocean Model. *J Adv Model Earth Sy*, **12**.

Bachman, S. D., D. P. Marshall, J. R. Maddison, and J. Mak, 2017: Evaluation of a scalar eddy transport coefficient based on geometric constraints. *Ocean Model*, **109,** 44-54.

Bleck, R., 2002: An Oceanic general circulation model framed in hybrid isopycnic-Cartesian coordinates (vol 4, pg 55, 2002). *Ocean Model*, **4,** 219-219.

Bleck, R., C. Rooth, D. M. Hu, and L. T. Smith, 1992: Salinity-Driven Thermocline Transients in a Wind-Forced and Thermohaline-Forced Isopycnic Coordinate Model of the North-Atlantic. *J Phys Oceanogr*, **22,** 1486-1505.

Booth, J., and I. Kamenkovich, 2008: Isolating the role of mesoscale eddies in mixing of a passive tracer in an eddy resolving model. *J Geophys Res-Oceans*, **113**.

683 Broecker, W. S., 1997: Thermohaline circulation, the Achilles heel of our climate system: Will
684 man-made CO2 upset the current balance? *Science*, **278,** 1582-1588.

685 Bryan, F., 1987: Parameter Sensitivity of Primitive Equation Ocean General-Circulation Models.
686 *J Phys Oceanogr*, **17,** 970-985.

687 Callies, J., R. Ferrari, J. M. Klymak, and J. Gula, 2015: Seasonality in submesoscale turbulence.
688 *Nat Commun*, **6**.

689 Cessi, P., and M. Fantini, 2004: The eddy-driven thermocline. *J Phys Oceanogr*, **34,** 2642-2658.

690 Chassignet, E. P., L. T. Smith, G. R. Halliwell, and R. Bleck, 2003: North Atlantic Simulations
691 with the Hybrid Coordinate Ocean Model (HYCOM): Impact of the vertical coordinate
692 choice, reference pressure, and thermobaricity. *J Phys Oceanogr*, **33,** 2504-2526.

693 Chelton, D. B., R. A. DeSzoeke, M. G. Schlax, K. El Naggar, and N. Siwertz, 1998:
694 Geographical variability of the first baroclinic Rossby radius of deformation. *J Phys*
695 *Oceanogr*, **28,** 433-460.

696 Doney, S. C., K. Lindsay, K. Caldeira, J. M. Campin, H. Drange, J. C. Dutay, M. Follows, Y.
697 Gao, A. Gnanadesikan, N. Gruber, A. Ishida, F. Joos, G. Madec, E. Maier-Reimer, J. C.
698 Marshall, R. J. Matear, P. Monfray, A. Mouchet, R. Najjar, J. C. Orr, G. K. Plattner, J.
699 Sarmiento, R. Schlitzer, R. Slater, I. J. Totterdell, M. F. Weirig, Y. Yamanaka, and A.
700 Yool, 2004: Evaluating global ocean carbon models: The importance of realistic physics.
701 *Global Biogeochem Cy*, **18**.

702 Dutay, J. C., J. L. Bullister, S. C. Doney, J. C. Orr, R. Najjar, K. Caldeira, J. M. Campin, H.
703 Drange, M. Follows, Y. Gao, N. Gruber, M. W. Hecht, A. Ishida, F. Joos, K. Lindsay, G.
704 Madec, E. Maier-Reimer, J. C. Marshall, R. J. Matear, P. Monfray, A. Mouchet, G. K.
705 Plattner, J. Sarmiento, R. Schlitzer, R. Slater, I. J. Totterdell, M. F. Weirig, Y. Yamanaka,
706 and A. Yool, 2002: Evaluation of ocean model ventilation with CFC-11: comparison of
707 13 global ocean models. *Ocean Model*, **4,** 89-120.

708 Fox-Kemper, B., R. Ferrari, and J. Pedlosky, 2003: On the indeterminacy of rotational and
709 divergent eddy fluxes. *J Phys Oceanogr*, **33,** 478-483.

710 Gent, P. R., and J. C. McWilliams, 1990: Isopycnal Mixing in Ocean Circulation Models. *J Phys*
711 *Oceanogr*, **20,** 150-155.

712 Gnanadesikan, A., 1999: A simple predictive model for the structure of the oceanic pycnocline.
713 *Science*, **283,** 2077-2079.

714 Gnanadesikan, A., D. Bianchi, and M. A. Pradal, 2013: Critical role for mesoscale eddy diffusion
715 in supplying oxygen to hypoxic ocean waters. *Geophys Res Lett*, **40,** 5194-5198.

716 Gnanadesikan, A., M. A. Pradal, and R. Abernathey, 2015: Isopycnal mixing by mesoscale
717 eddies significantly impacts oceanic anthropogenic carbon uptake. *Geophys Res Lett*, **42,**
718 4249-4255.

719 Gnanadesikan, A., J. P. Dunne, R. M. Key, K. Matsumoto, J. L. Sarmiento, R. D. Slater, and P.
720 S. Swathi, 2004: Oceanic ventilation and biogeochemical cycling: Understanding the
721 physical mechanisms that produce realistic distributions of tracers and productivity.
722 *Global Biogeochem Cy*, **18**.

723 Grist, J. P., R. Marsh, and S. A. Josey, 2009: On the Relationship between the North Atlantic
724 Meridional Overturning Circulation and the Surface-Forced Overturning Streamfunction.
725 *J Climate*, **22,** 4989-5002.

726 Haigh, M., and P. Berloff, 2021: On co-existing diffusive and anti-diffusive tracer transport by
727 oceanic mesoscale eddies. *Ocean Model*, **168**.

728 Haigh, M., L. Sun, I. Shevchenko, and P. Berloff, 2020: Tracer-based estimates of eddy-induced
729 diffusivities. *Deep-Sea Res Pt I*, **160**.

730 Haigh, M., L. L. Sun, J. C. McWilliams, and P. Berloff, 2021a: On eddy transport in the ocean.
731 Part II: The advection tensor. *Ocean Model*, **165**.

732 Haigh, M., L. L. Sun, J. C. McWilliams, and P. Berloff, 2021b: On eddy transport in the ocean.
733 Part I: The diffusion tensor. *Ocean Model*, **164**.

734 Haine, T. W. N., and T. M. Hall, 2002: A generalized transport theory: Water-mass composition
735 and age. *J Phys Oceanogr*, **32,** 1932-1946.

736 Halliwell, G. R., 2004: Evaluation of vertical coordinate and vertical mixing algorithms in the
737 HYbrid-Coordinate Ocean Model (HYCOM). *Ocean Model*, **7,** 285-322.

738 Han, M., I. Kamenkovich, T. Radko, and W. E. Johns, 2013: Relationship between Air-Sea
739 Density Flux and Isopycnal Meridional Overturning Circulation in a Warming Climate. *J*
740 *Climate*, **26,** 2683-2699.

741 Henning, C. C., and G. K. Vallis, 2004: The effects of mesoscale eddies on the main subtropical
742 thermocline. *J Phys Oceanogr*, **34,** 2428-2443.

743 Holzer, M., and T. M. Hall, 2000: Transit-time and tracer-age distributions in geophysical flows.
744 *J Atmos Sci*, **57,** 3539-3558.

745 Huang, B. Y., P. H. Stone, A. P. Sokolov, and I. V. Kamenkovich, 2003: Ocean heat uptake in
746 transient climate change: Mechanisms and uncertainty due to subgrid-scale eddy mixing.
747 *J Climate*, **16,** 3344-3356.

748 Jayne, S. R., and J. Marotzke, 2002: The oceanic eddy heat transport. *J Phys Oceanogr*, **32,**
749 3328-3345.

750 Kamenkovich, I., and T. Radko, 2011: Role of the Southern Ocean in setting the Atlantic
751 stratification and meridional overturning circulation. *J Mar Res*, **69,** 277-308.

752 Kamenkovich, I., P. Berloff, and J. Pedlosky, 2009: Anisotropic Material Transport by Eddies
753 and Eddy-Driven Currents in a Model of the North Atlantic. *J Phys Oceanogr*, **39,** 3162-
754 3175.

755 Kamenkovich, I., I. I. Rypina, and P. Berloff, 2015: Properties and Origins of the Anisotropic
756 Eddy-Induced Transport in the North Atlantic. *J Phys Oceanogr*, **45,** 778-791.

757 Kamenkovich, I., Z. Garraffo, R. Pennel, and R. A. Fine, 2017: Importance of mesoscale eddies
758 and mean circulation in ventilation of the Southern Ocean. *J Geophys Res-Oceans*, **122,**
759 2724-2741.

760 Kamenkovich, I., P. Berloff, M. Haigh, L. L. Sun, and Y. Y. Lu, 2021: Complexity of Mesoscale
761 Eddy Diffusivity in the Ocean. *Geophys Res Lett*, **48**.

762 Khatiwala, S., M. Visbeck, and P. Schlosser, 2001: Age tracers in an ocean GCM. *Deep-Sea Res*
763 *Pt I*, **48,** 1423-1441.

764 Khatiwala, S., F. Primeau, and T. Hall, 2009: Reconstruction of the history of anthropogenic
765 CO2 concentrations in the ocean. *Nature*, **462,** 346-U110.

766 Kostov, Y., K. C. Armour, and J. Marshall, 2014: Impact of the Atlanticmeridional overturning
767 circulation on ocean heat storage and transient climate change. *Geophys Res Lett*, **41,**
768 2108-2116.

769 Kuhlbrodt, T., and J. M. Gregory, 2012: Ocean heat uptake and its consequences for the
770 magnitude of sea level rise and climate change. *Geophys Res Lett*, **39**.

771 Large, W. G., J. C. Mcwilliams, and S. C. Doney, 1994: Oceanic Vertical Mixing - a Review and
772 a Model with a Nonlocal Boundary-Layer Parameterization. *Rev Geophys*, **32,** 363-403.

773 Lau, N. C., and J. M. Wallace, 1979: Distribution of Horizontal Transports by Transient Eddies
774 in the Northern Hemisphere Wintertime Circulation. *J Atmos Sci*, **36,** 1844-1861.

775 Ledwell, J. R., A. J. Watson, and C. S. Law, 1993: Evidence for Slow Mixing across the
776 Pycnocline from an Open-Ocean Tracer-Release Experiment. *Nature*, **364,** 701-703.

777 Li, Z. J., Y. Chao, and J. C. McWilliams, 2006: Computation of the streamfunction and velocity
778 potential for limited and irregular domains. *Mon Weather Rev*, **134,** 3384-3394.

779 Lumpkin, R., and K. Speer, 2007: Global ocean meridional overturning. *J Phys Oceanogr*, **37,**
780 2550-2562.

781 Maddison, J. R., D. P. Marshall, and J. Shipton, 2015: On the dynamical influence of ocean eddy
782 potential vorticity fluxes. *Ocean Model*, **92,** 169-182.

783 Maltrud, M., F. Bryan, and S. Peacock, 2010: Boundary impulse response functions in a century-
784 long eddying global ocean simulation. *Environ Fluid Mech*, **10,** 275-295.

785 Marshall, J., and G. Shutts, 1981: A Note on Rotational and Divergent Eddy Fluxes. *J Phys*
786 *Oceanogr*, **11,** 1677-1680.

787 Marshall, J., and T. Radko, 2003: Residual-mean solutions for the Antarctic Circumpolar Current
788 and its associated overturning circulation. *J Phys Oceanogr*, **33,** 2341-2354.

789 Marshall, J., J. R. Scott, K. C. Armour, J. M. Campin, M. Kelley, and A. Romanou, 2015: The
790 ocean's role in the transient response of climate to abrupt greenhouse gas forcing. *Clim*
791 *Dynam*, **44,** 2287-2299.

792 Maximenko, N. A., O. V. Melnichenko, P. P. Niiler, and H. Sasaki, 2008: Stationary mesoscale
793 jet-like features in the ocean. *Geophys Res Lett*, **35**.

794 Peacock, S., and M. Maltrud, 2006: Transit-time distributions in a global ocean model. *J Phys*
795 *Oceanogr*, **36,** 474-495.

796 Radko, T., and J. Marshall, 2004: The leaky thermocline. *J Phys Oceanogr*, **34,** 1648-1662.

797 Radko, T., I. Kamenkovich, and P. Y. Dare, 2008: Inferring the Pattern of the Oceanic
798 Meridional Transport from the Air-Sea Density Flux. *J Phys Oceanogr*, **38,** 2722-2738.

799 Roberts, M. J., and D. P. Marshall, 2000: On the validity of downgradient eddy closures in ocean
800 models. *J Geophys Res-Oceans*, **105,** 28613-28627.

801 Rypina, I. I., I. Kamenkovich, P. Berloff, and L. J. Pratt, 2012: Eddy-Induced Particle Dispersion
802 in the Near-Surface North Atlantic. *J Phys Oceanogr*, **42,** 2206-2228.

803 Samelson, R. M., 2004: Simple mechanistic models of middepth meridional overturning. *J Phys*
804 *Oceanogr*, **34,** 2096-2103.

805 Sen Gupta, A., and M. H. England, 2004: Evaluation of interior circulation in a high-resolution
806 global ocean model. Part I: Deep and bottom waters. *J Phys Oceanogr*, **34,** 2592-2614.

807 Sevellec, F., and A. V. Fedorov, 2011: Stability of the Atlantic meridional overturning
808 circulation and stratification in a zonally averaged ocean model: Effects of freshwater
809 flux, Southern Ocean winds, and diapycnal diffusion. *Deep-Sea Res Pt Ii*, **58,** 1927-1943.

Shevchenko, I. V., and P. S. Berloff, 2015: Multi-layer quasi-geostrophic ocean dynamics in Eddy-resolving regimes. *Ocean Model*, **94,** 1-14.

Smeed, D. A., G. D. McCarthy, S. A. Cunningham, E. Frajka-Williams, D. Rayner, W. E. Johns, C. S. Meinen, M. O. Baringer, B. I. Moat, A. Duchez, and H. L. Bryden, 2014: Observed decline of the Atlantic meridional overturning circulation 2004-2012. *Ocean Sci*, **10,** 29-38.

Stouffer, R. J., J. Yin, J. M. Gregory, K. W. Dixon, M. J. Spelman, W. Hurlin, A. J. Weaver, M. Eby, G. M. Flato, H. Hasumi, A. Hu, J. H. Jungclaus, I. V. Kamenkovich, A. Levermann, M. Montoya, S. Murakami, S. Nawrath, A. Oka, W. R. Peltier, D. Y. Robitaille, A. Sokolov, G. Vettoretti, and S. L. Weber, 2006: Investigating the causes of the response of the thermohaline circulation to past and future climate changes. *J Climate*, **19,** 1365-1387.

Sun, L. L., M. Haigh, I. Shevchenko, P. Berloff, and I. Kamenkovich, 2021: On non-uniqueness of the mesoscale eddy diffusivity. *J Fluid Mech*, **920**.

Sun, S., and R. Bleck, 2001: Thermohaline circulation studies with an Isopycnic Coordinate Ocean Model. *J Phys Oceanogr*, **31,** 2761-2782.

Sun, S., R. Bleck, C. Rooth, J. Dukowicz, E. Chassignet, and P. Killworth, 1999: Inclusion of thermobaricity in isopycnic-coordinate ocean models. *J Phys Oceanogr*, **29,** 2719-2729.

Toggweiler, J. R., and B. Samuels, 1998: On the ocean's large-scale circulation near the limit of no vertical mixing. *J Phys Oceanogr*, **28,** 1832-1852.

Toole, J. M., K. L. Polzin, and R. W. Schmitt, 1994: Estimates of Diapycnal Mixing in the Abyssal Ocean. *Science*, **264,** 1120-1123.

Tozuka, T., and M. F. Cronin, 2014: Role of mixed layer depth in surface frontogenesis: The Agulhas Return Current front. *Geophys Res Lett*, **41,** 2447-2453.

Waterman, S., N. G. Hogg, and S. R. Jayne, 2011: Eddy-Mean Flow Interaction in the Kuroshio Extension Region. *J Phys Oceanogr*, **41,** 1182-1208.

Waugh, D. W., and T. M. Hall, 2005: Propagation of tracer signals in boundary currents. *J Phys Oceanogr*, **35,** 1538-1552.

Wolfe, C. L., and P. Cessi, 2010: What Sets the Strength of the Middepth Stratification and Overturning Circulation in Eddying Ocean Models? *J Phys Oceanogr*, **40,** 1520-1538.

Yeager, S., and G. Danabasoglu, 2014: The Origins of Late-Twentieth-Century Variations in the Large-Scale North Atlantic Circulation. *J Climate*, **27,** 3222-3247.

842 Zalesak, S. T., 1979: Fully Multidimensional Flux-Corrected Transport Algorithms for Fluids. *J*
843 *Comput Phys*, **31,** 335-362.

844